

# High-temperature observation of intralayer, interlayer, and Rydberg excitons in bulk van der Waals alloy single crystals

Pravrati Taank,<sup>1</sup> Asif Ali,<sup>1</sup> Aravind Raji,<sup>1</sup> Ajay K. Poonia,<sup>1</sup>  
Matthew C. Beard,<sup>2</sup> Ravi Shankar Singh,<sup>1,\*</sup> and K. V. Adarsh<sup>1,†</sup>

<sup>1</sup>*Department of Physics, Indian Institute of Science Education and Research Bhopal, Bhopal 462066, India*

<sup>2</sup>*Chemistry & Nanoscience Center, National Renewable Energy Laboratory; Golden, Colorado 80401, USA*

Transition metal dichalcogenides (TMDs) exhibit remarkable optical properties due to the diverse number of strongly bound excitons, which can be fine-tuned by alloying. Despite a flurry of research activity in characterizing these excitons, a comprehensive and profound understanding of their behavior with temperature is lacking. Here, we report the rich spectrum of excitonic features within bulk van der Waals alloy  $\text{Mo}_{0.5}\text{W}_{0.5}\text{S}_2$  and  $\text{Mo}_{0.5}\text{W}_{0.5}\text{Se}_2$  single crystals through temperature-dependent reflectance spectroscopy and first-principle calculations. We observed Rydberg excitons and interlayer excitons in both the single crystals. Notably, we provide the first experimental evidence of highly energetic  $A'$  and  $B'$  excitons in  $\text{Mo}_{0.5}\text{W}_{0.5}\text{S}_2$  at room temperature. The strong carrier-phonon scattering significantly broadens the  $A'$ ,  $B'$  and interlayer excitons at room temperature in bulk  $\text{Mo}_{0.5}\text{W}_{0.5}\text{S}_2$  single crystal compared to its selenide. Our findings, supported by density functional theory and Bethe-Salpeter equation calculations, signify the crucial role of carrier-phonon interactions. These results open pathways for next-generation optoelectronic devices and quantum technologies operating at high temperature.

Transition metal dichalcogenides (TMDs) have emerged as a new class of semiconductors for a wide range of applications in electronics and optoelectronics because of their remarkable properties like sizable bandgaps [1], substantial spin-valley coupling [2, 3], spin-layer locking [4, 5], reduced dielectric screening [1, 6], and strong Coulomb interactions resulting in the high binding energy of excitons [2, 6, 7]. These characteristics contribute to TMD's rich and diverse landscape of excitonic transitions, positioning them at the forefront of optical technology, particularly in the domains of spintronics [8] and valleytronics [9]. For example, large spin-orbit coupling (SOC) in TMDs splits the valance and conduction bands at the K-valley. This splitting results in the formation of low-energy intralayer A and B excitons and their excitonic Rydberg series [2, 10–13]. Another example is interlayer excitons (IXs) at the K-valleys, where electrons and holes residing in separate layers bind to form excitons based on spin-valley and spin-layer selection rules [3–5, 14]. Also, some of the TMDs, such as, selenides [15–18] and tellurides [15, 18], show highly energetic  $A'$  and  $B'$  excitons, however, these excitons are not observed in sulfides. For more details see Table S1 in Supplemental Material (SM) [19] and in Refs. [3, 4, 15–18, 20–26]. Overall, all these diverse excitons present in TMDs offer a wide range of potential optoelectronic applications, including optical quantum sensing [27], Bose-Einstein condensation [5, 28], optical switching [12], and quantum information technology [29, 30].

TMDs present unique opportunities for alloying through isoelectronic substitution of transition metal (M)

or chalcogen (X) atoms, resulting in minimal lattice strain and the formation of quasi-binary alloys that preserve the  $\text{MX}_2$  structure [31–34]. This structural stability allows diverse excitons within these quasi-binary alloys, mirroring those found in their binary counterparts. In principle, they can provide more fundamental insights than binary TMDs. For example, the right choice of atoms in an alloy offers a platform to tune the SOC and carrier-phonon scattering to explore a broader spectrum of excitons. Likewise, how the diverse excitons behave at different temperatures in TMDs is still lacking, which is essential for potential device applications.

Here, we present a comprehensive understanding of diverse excitonic features observed in the optical reflectance spectra of bulk  $\text{Mo}_{0.5}\text{W}_{0.5}\text{S}_2$  and  $\text{Mo}_{0.5}\text{W}_{0.5}\text{Se}_2$  alloy single crystals using temperature-dependent reflectance spectroscopy and first-principle calculations. In our experiments, we observed the Rydberg excitons of A exciton ( $1s$  ground state) up to  $n=4$  quantum number i.e.,  $2s$ ,  $3s$  and  $4s$  in  $\text{Mo}_{0.5}\text{W}_{0.5}\text{S}_2$  single crystal. Another noteworthy findings are the first experimental observation of  $A'$  and  $B'$  excitons in transition metal sulfides at room temperature, and the observation of IX between A and B excitons in both single crystals. The strong carrier-phonon scattering significantly broadens these excitons at room temperature in bulk  $\text{Mo}_{0.5}\text{W}_{0.5}\text{S}_2$  single crystal compared to its selenide. Furthermore, our theoretical calculations concur well with the experimental results.

Bulk  $\text{Mo}_{0.5}\text{W}_{0.5}\text{S}_2$  and  $\text{Mo}_{0.5}\text{W}_{0.5}\text{Se}_2$  alloy single crystals used in this study were procured from HQ Graphene. These crystals underwent extensive characterization (X-ray diffraction, scanning electron microscopy, energy-dispersive X-ray spectra and X-ray photoemission spectroscopy) to assess their structural and compositional properties. Details are provided in SM [19]. Our measurements reveal the high quality and chemical purity of

\* [rssingh@iiserb.ac.in](mailto:rssingh@iiserb.ac.in)

† [adarsh@iiserb.ac.in](mailto:adarsh@iiserb.ac.in)

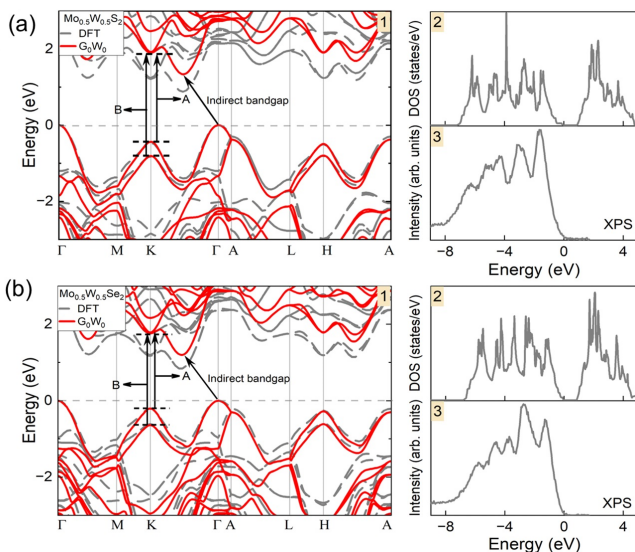


FIG. 1. Electronic band structure using DFT and  $G_0W_0$  calculations of bulk (a)  $\text{Mo}_{0.5}\text{W}_{0.5}\text{S}_2$  and (b)  $\text{Mo}_{0.5}\text{W}_{0.5}\text{Se}_2$ , (panel 1). The grey dashed line illustrates the Fermi levels. Panel 2 shows the calculated total DOS and panel 3 shows the room temperature experimental valence band spectra from XPS for both single crystals.

the single crystals.

Since the crystalline TMD of  $\text{MX}_2$  displays large exciton binding energy and oscillator strength, we expect similar features in the optical and charge-transport properties of the alloy single crystals. For the identification of such diverse exciton species, we conducted a thorough investigation of the electronic structures of bulk  $\text{Mo}_{0.5}\text{W}_{0.5}\text{S}_2$  and  $\text{Mo}_{0.5}\text{W}_{0.5}\text{Se}_2$  within density functional theory (DFT) using the projector-augmented wave method [35] as implemented in the Vienna Ab-Initio Simulation Package (VASP) [36] with the exchange-correlation functional of Perdew-Burke-Ernzerhof (PBE) [37]. Experimental lattice parameters were used for all calculations, and virtual crystal approximation (VCA) [38] was employed to represent the alloy compositions. The total density of state (DOS) calculations were done using the tetrahedron method. More details are in SM [19] and in Refs. [39–42]. The calculated electronic band structures and DOS of  $\text{Mo}_{0.5}\text{W}_{0.5}\text{S}_2$  and  $\text{Mo}_{0.5}\text{W}_{0.5}\text{Se}_2$  are shown in Figs. 1(a, b) in panels 1 and 2. Our calculations reveal that both alloys exhibit an indirect bandgap nature, with the respective valence band maximum (VBM) situated at the  $\Gamma$  point and the conduction band minimum located between the K- $\Gamma$  points in both DFT (grey) and  $G_0W_0$  (red) calculations. Additionally, the introduction of SOC leads to a splitting of the VBM, resulting in the first direct bandgap at the K point and the second direct bandgap at the H point. Our theoretical findings are consistent with the previously reported calculations in  $\text{MoS}_2$  [43] and  $\text{WS}_2$  [44] and highlight the significant contribution of transition metal d-electrons to the band structure of these bulk alloy single crystals.

To understand the electronic structure of these sys-

tems, we compared the calculated DOS (panels 2) with the experimental valence band (panels 3) for bulk  $\text{Mo}_{0.5}\text{W}_{0.5}\text{S}_2$  and  $\text{Mo}_{0.5}\text{W}_{0.5}\text{Se}_2$  in Figs. 1(a, b), respectively. The observed valence band spectrum at room temperature exhibits semiconducting behavior with zero intensity at the Fermi level. The experimental valence band spectrum reveals five distinct features for  $\text{Mo}_{0.5}\text{W}_{0.5}\text{S}_2$  and  $\text{Mo}_{0.5}\text{W}_{0.5}\text{Se}_2$ . These features reproduced in the calculated DOS are in good agreement with experimental valence band spectra. Furthermore, we compare the band dispersion with room temperature angle-resolved photoemission spectroscopy (ARPES), revealing the SOC-driven K-valley splitting of  $\sim 0.37$  eV in  $\text{Mo}_{0.5}\text{W}_{0.5}\text{Se}_2$ , as shown in Fig. S6 [19]. The DFT calculated band structure overlaid over the ARPES spectrum (Fig. S6 [19]) shows a good agreement suggesting that DFT with VCA is sufficient enough to capture the main features of the valence band in the case of bulk alloy single crystals.

Bulk  $\text{Mo}_{0.5}\text{W}_{0.5}\text{S}_2$  and  $\text{Mo}_{0.5}\text{W}_{0.5}\text{Se}_2$  exhibit atomic stacking of  $YY^*$  type, leading to 2H symmetry, as illustrated in Fig. S7 [19]. These bulk single crystals demonstrate a wide range of bright intralayer and interlayer excitons with notably high oscillator strengths. The former obeys the spin-valley selection rules, while the latter follows the spin-layer selection rules [4, 45]. We conducted temperature-dependent reflectance spectroscopy to investigate these diverse optically active excitons and their impact on the optical properties of these single crystals. Detailed experimental procedure is in SM [19]. Figs. 2(a, b) display the reflectance spectra at a high temperature of 80 K for bulk  $\text{Mo}_{0.5}\text{W}_{0.5}\text{S}_2$  and  $\text{Mo}_{0.5}\text{W}_{0.5}\text{Se}_2$  single crystals, respectively. These spectra clearly demonstrate the presence of multiple optically active excitons.

To gain a deeper understanding, we conducted theoretical calculations of the absorption spectra by incorporating electron-hole interactions and solving the Bethe-Salpeter equation (BSE) with the Tamm-Dancoff approximation [46]. We considered the eight lowest conduction and eight highest valence bands for the BSE calculations. In Figs. 2(c, d), we present the theoretically calculated absorption spectra of bulk  $\text{Mo}_{0.5}\text{W}_{0.5}\text{S}_2$  and  $\text{Mo}_{0.5}\text{W}_{0.5}\text{Se}_2$ , and the spectra are well in agreement with the experimental results in Figs. 2(a, b). These diverse spectral features observed in the experimental and theoretical spectra can be attributed to a range of excitonic transitions within the Brillouin zone, and their assignments are discussed in the following paragraphs.

First, we discuss the low-energy intralayer excitons, A and B, which are observed at  $\sim 1.915$  eV and  $\sim 2.221$  eV for  $\text{Mo}_{0.5}\text{W}_{0.5}\text{S}_2$  and at  $\sim 1.603$  eV and  $\sim 1.955$  eV for  $\text{Mo}_{0.5}\text{W}_{0.5}\text{Se}_2$ . The A and B excitons originate from the splitting of the VBM due to strong SOC at K point of the Brillouin zone [29, 47]. The energy difference between the A and B excitons, which is an indicator of the strength of SOC [21], is  $\sim 306$  and  $\sim 352$  meV in  $\text{Mo}_{0.5}\text{W}_{0.5}\text{S}_2$  and  $\text{Mo}_{0.5}\text{W}_{0.5}\text{Se}_2$ , respectively. These values are in good agreement with our theoretical calculations, for the respective samples  $\sim 323$  and  $\sim 378$  meV. The fact that  $\text{Mo}_{0.5}\text{W}_{0.5}\text{Se}_2$  exhibits a stronger SOC, as indicated by

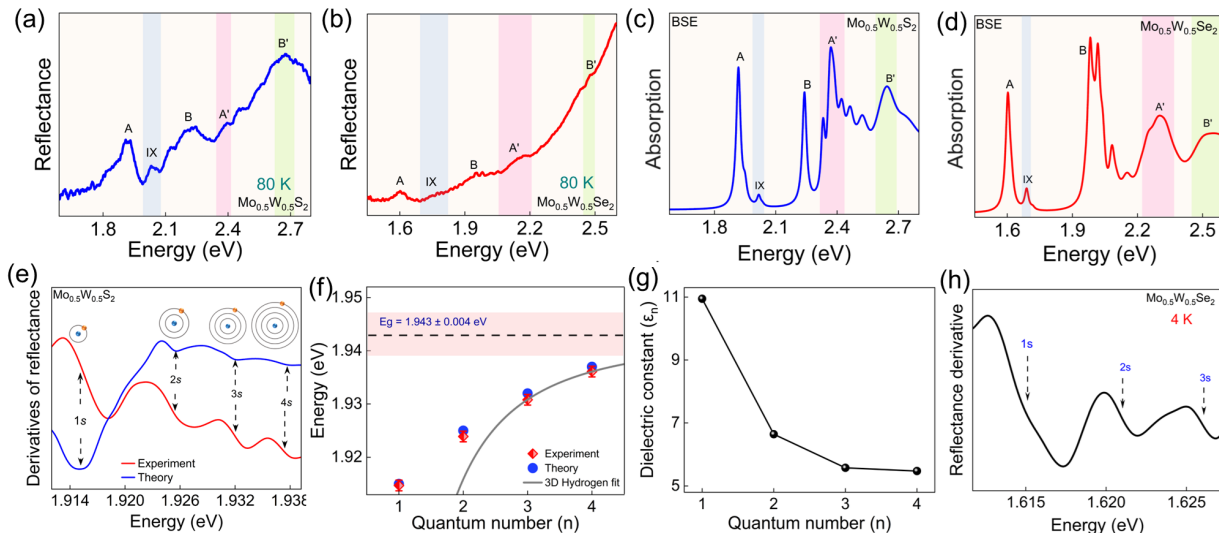


FIG. 2. Reflectance spectrum at 80 K for bulk (a)  $\text{Mo}_{0.5}\text{W}_{0.5}\text{S}_2$  and (b)  $\text{Mo}_{0.5}\text{W}_{0.5}\text{S}_2$  single crystals. The blue, pink, and green regions show the interlayer (IX),  $A'$  and  $B'$  excitons, respectively. The theoretical absorption spectrum calculated using BSE for bulk (c)  $\text{Mo}_{0.5}\text{W}_{0.5}\text{S}_2$  and (d)  $\text{Mo}_{0.5}\text{W}_{0.5}\text{S}_2$ . (e) The first derivative of the experimentally measured reflectance spectrum and the second derivative of the theoretically calculated BSE absorption spectrum of bulk  $\text{Mo}_{0.5}\text{W}_{0.5}\text{S}_2$  single crystal at 80 K. The peaks represent the Rydberg excitons up to  $4s$  states, which follow Bohr's atomic model as shown schematically. Where blue and yellow balls are the nucleus (hole here) and the electron, respectively. The theoretical absorption spectra have been shifted by  $\sim 0.26$  eV for better comparison with the experimental spectra. (f) Experimentally and theoretically obtained the transition energies of the Rydberg series as a function of quantum number ( $n$ ). The  $n=3,4$  peaks follow the 3D hydrogen model and the fit is represented by the grey line. The black dashed line and pink shaded area show the estimated  $E_g$  and uncertainty in the  $E_g$  value, respectively. (g) Calculated dielectric constants  $\epsilon_n$  as a function of  $n$ . (h) The second derivative of the reflectance spectrum of bulk  $\text{Mo}_{0.5}\text{W}_{0.5}\text{S}_2$  single crystal at 4 K shows Rydberg series up to  $n=3$ .

the larger energy difference between A and B excitons, compared to  $\text{Mo}_{0.5}\text{W}_{0.5}\text{S}_2$  is due to the heavier chalcogen atom. This is further supported by the band structure calculations presented in Fig. 1. The A and B exciton positions in our BSE calculation are slightly overestimated than the experimental values due to overestimation of bandgap in  $G_0W_0$  calculations.

To unravel the subtle characteristics of other excitonic transitions between A and B excitons, we have taken the first derivative of the reflectance spectrum of  $\text{Mo}_{0.5}\text{W}_{0.5}\text{S}_2$  single crystal and plotted it in Fig. 2(e). On the higher-energy side of the A exciton known as the  $1s$  ground state, we have obtained three additional peaks in Fig. 2(e). The intriguing aspect here lies in the gradual and continuous decrease in both peak intensities and energy separations as we move to higher energies is analogous to the excitonic Rydberg series [2]. So, we associate these fine structures as the excited states of A exciton up to  $n=4$  quantum number, i.e.,  $2s$ ,  $3s$ , and  $4s$ , since the energy separation and spectral weights resemble that of a hydrogen atom. Further, the transitions manifest as peaks situated between the  $1s$  ground state and the quasiparticle bandgap, as previously discussed in monolayer TMDs [2, 11, 48]. These  $s$ -like state transitions are dipole-allowed and thus can be probed by linear optical spectroscopy [12]. Notably, our theoretical calculations also corroborate this trend. The second derivative of the theoretically calculated absorption spectrum exhibits a similar pattern, with the minima in the curve pinpoint-

ing the energy positions of the Rydberg excitons. We observed similar features using the first derivative of the reflectance data (Fig. S9 [19]); however, the utilization of the second derivative enhances resolution, providing a more precise analysis. For clarity, we have outlined a schematic diagram in Fig. 2(e), aligning with Bohr's atomic model, where the electron resides in the corresponding shell. Furthermore, we have extracted the energy positions of these Rydberg excitons from the points of inflection of Fig. 2(e), and these positions are presented in Fig. 2(f) for a comprehensive view of the findings. Similar results are also obtained at 4 K (Fig. S10 [19]); however, Rydberg excitons disappear as temperature increases beyond 80 K due to large carrier-phonon scattering [49]. Further, we observed the Rydberg series of excitons in  $\text{Mo}_{0.5}\text{W}_{0.5}\text{Se}_2$  at 4 K (Fig. 2(h)).

From the exciton Rydberg series of the single crystal, we have computed the exciton binding energy using the formula typically used for three-dimensional (3D) Wannier excitons [50, 51], given by  $E_b^n = E_g - (R_y^*/n^2)$ . Here,  $E_b^n$ ,  $E_g$ , and  $R_y^*$  are the binding energy of  $n^{\text{th}}$  exciton, quasiparticle bandgap, and effective Rydberg constant, respectively. We have used only  $n=3$  and 4 Rydberg excitons for fitting the data, since they are hydrogenic in nature, which is discussed later. The extracted value of  $E_g = 1.943 \pm 0.004$  eV (black dashed line in Fig. 2(f)) and  $E_b (= E_g - E_{A(1s)}) = 28 \pm 4$  meV. Notably, our observed binding energy values are similar to those of GaSe [52], GaN [53] and ZnO [54] bulk single crystals, but at

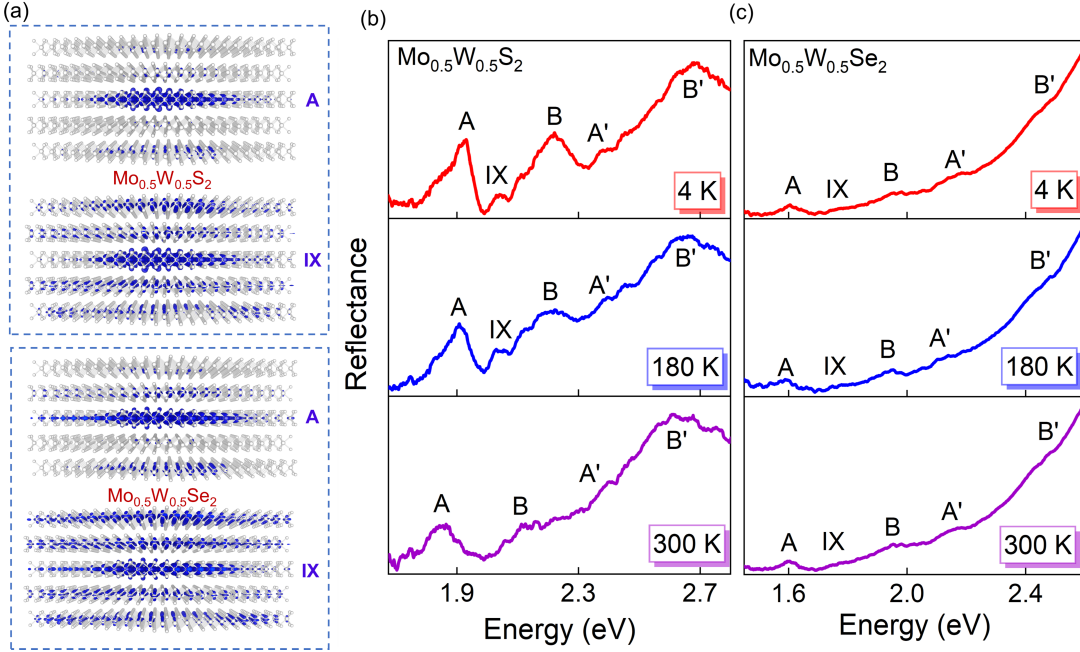


FIG. 3. (a) Spatial distribution of excitons shows nature of A (intralayer) and IX excitons for  $\text{Mo}_{0.5}\text{W}_{0.5}\text{S}_2$  (Top panel) and  $\text{Mo}_{0.5}\text{W}_{0.5}\text{Se}_2$  (Bottom panel). Reflectance spectra as a function of temperature for bulk (b)  $\text{Mo}_{0.5}\text{W}_{0.5}\text{S}_2$  and (c)  $\text{Mo}_{0.5}\text{W}_{0.5}\text{Se}_2$  single crystals.

least an order of magnitude smaller than monolayer  $\text{MoS}_2$  and  $\text{WS}_2$  [2, 10] due to the significantly large screening effect in the bulk material. To explain the observed non-hydrogenic behavior, we determined the non-uniform dielectric constant  $\epsilon_n = \sqrt{\mu e^4 / (2\hbar^2 E_b^{(n)} n^2)}$  experienced by the Rydberg excitons [2], where  $\mu$  represents the exciton reduced mass in terms of the electron rest mass ( $m_0$ ) and is found to be  $0.2471m_0$ , as estimated by DFT calculations at the K-valley. Our results demonstrate a drastic reduction in  $\epsilon_n$  for  $n = 1$  and 2, while it remains nearly constant for  $n = 3, 4$  Rydberg excitons as shown in Fig. 2(g). This justifies the use of the 3D hydrogenic model for fitting  $n = 3, 4$ , and the deviation from the hydrogenic model for  $n = 1, 2$  can be attributed to the antiscreening effect, consistent with previous reports in other TMDs [2, 10] and semiconductors [55, 56].

Another remarkable observation of our study is the identification of a distinctive spectral feature appearing at high energy to the A exciton by  $\sim 114$  meV in  $\text{Mo}_{0.5}\text{W}_{0.5}\text{S}_2$  and  $\sim 156$  meV in  $\text{Mo}_{0.5}\text{W}_{0.5}\text{Se}_2$ , which is well below the B exciton within the reflectance spectrum, see Figs. 2(a, b). We assign these features to the direct IXs. Notably, our temperature-dependent studies presented in Fig. 3(b) show the weakening of IX peak after 180 K in  $\text{Mo}_{0.5}\text{W}_{0.5}\text{S}_2$ , nevertheless, in  $\text{Mo}_{0.5}\text{W}_{0.5}\text{Se}_2$ , we could observe IX up to room temperature (Fig. 3(c)). In contrast to the direct intralayer A exciton, these IXs exhibit reduced oscillator strength, strong dipole-dipole interactions, and lower binding energy. To provide a clearer understanding of the underlying mechanism, we have shown the schematic representation of band structure (Fig. S11 [19]) and spin configurations of IXs at

the K-valley in the  $YY^*$  stacked bulk alloy single crystal, considering two adjacent layers as depicted in Fig. S12 [19]. At each K point, the band structure is composed of SOC split valence bands  $V_1^{(\uparrow)}$  and  $V_2^{(\downarrow)}$ , as well as conduction bands  $C_1^{(\uparrow)}$ , and  $C_2^{(\downarrow)}$  in layer 1 and with spin inversion in layer 2, referred to as spin-layer locking [4, 5]. Due to spin conservation in optical dipole transitions, IXs form within the same spin-oriented bands of adjacent layers [4]. To confirm that the assigned peaks are IXs, we have calculated the exciton wave function which shows the charge density plot of the electron by keeping the hole position fixed very close to the transition metal position, as shown in Fig. 3(a). As can be noticed from the figure that the A exciton is confined within one layer, suggesting intralayer exciton like nature. On the other hand, IX is delocalized in neighboring layers, indicating interlayer characteristics.

Likewise, we observe IX in  $\text{Mo}_{0.5}\text{W}_{0.5}\text{Se}_2$  single crystal, see Fig. 3(c); however, a relatively broad and weak feature of IX is detected. This can be attributed to the weak interlayer coupling between the bands due to the larger spin-orbit splitting of the electronic bands [3, 57], i.e.,  $\text{Mo}_{0.5}\text{W}_{0.5}\text{Se}_2$  exhibits larger spin-orbit splitting than  $\text{Mo}_{0.5}\text{W}_{0.5}\text{S}_2$ , see Figs. 3(b, c). This fosters stronger interlayer coupling, forming IX of larger oscillator strength in  $\text{Mo}_{0.5}\text{W}_{0.5}\text{S}_2$  compared to  $\text{Mo}_{0.5}\text{W}_{0.5}\text{Se}_2$ . In contrast to  $\text{Mo}_{0.5}\text{W}_{0.5}\text{Se}_2$ , this IX becomes less discernible at room temperature in  $\text{Mo}_{0.5}\text{W}_{0.5}\text{S}_2$ . This may be due to the delocalization of carriers caused by high carrier-phonon scattering in sulfides, as noticed from high LO phonon energy in our phonon calculations discussed later. Further, we extended our analysis to include mono-

layers for the completeness of our theoretical calculation. As expected, in the case of monolayers, we did not observe any signature of the IX, see Fig. S13 [19].

Another noteworthy observation of our study is the demonstration of highly energetic  $A'$  and  $B'$  excitons originating from SOC split valance band at K-valley ( $V_1$  and  $V_2$ ) to the higher conduction band since the energy separation of these features are same as that of  $A$  and  $B$  excitons (see Fig. S11 [19]). While the experimental identifications of these  $A'$  and  $B'$  excitons have been previously reported in materials like  $\text{MoSe}_2$  [18],  $\text{WSe}_2$  [16, 17], and  $\text{MoTe}_2$  [15, 18], it is important to note that their presence has not yet been experimentally demonstrated in any sulfide TMDs in monolayer or bulk, despite the theoretical predictions [7, 58]. The theoretical analysis suggests that the large size of anion atoms is not only responsible for the observation of  $A'$  and  $B'$  excitons but also for influencing the electron-phonon interactions depending on the excitonic energies [7]. This means at higher temperatures, electron-phonon interactions strongly affect the higher-energy excitons than the lower-energy excitons. As a result, higher energy excitonic peaks merge into a much broader peak and so could not be resolved in the experiments at relatively high temperatures. We conducted comprehensive temperature-dependent reflectance measurements from 4 to 300 K to address this, as presented in Figs. 3(b, c). This analysis revealed that at the lowest temperature of 4 K, we could distinctly observe the sharp  $A'$  and  $B'$  excitons in bulk  $\text{Mo}_{0.5}\text{W}_{0.5}\text{S}_2$  single crystal. However, as the temperature increased, they coalesced into much broader peaks and become less prominent at room temperature. Contrastingly,  $A'$  and  $B'$  excitons are observed in bulk  $\text{Mo}_{0.5}\text{W}_{0.5}\text{Se}_2$  single crystal are less affected with temperature, Fig. 3(c). To understand the mechanism and role played by phonons in the broadening of  $A'$  and  $B'$  excitons, we have calculated the phonon dispersion

curves of both alloys in Fig. S14 [19]. More details are in SM [19] and Refs. [59–61]. Due to the heavier atomic weight of Se atoms,  $\text{Mo}_{0.5}\text{W}_{0.5}\text{Se}_2$  phonon bands are shifted downwards to the lower frequencies compared to their sulfides. This signifies that carrier-phonon interactions become more significant in  $\text{Mo}_{0.5}\text{W}_{0.5}\text{S}_2$  due to high LO phonon energy of  $\sim 45$  meV in comparison to  $\text{Mo}_{0.5}\text{W}_{0.5}\text{Se}_2$  ( $\sim 32$  meV). As a result, highly energetic  $A'$  and  $B'$  excitons in  $\text{Mo}_{0.5}\text{W}_{0.5}\text{S}_2$  are becoming much broader and weaker at higher temperatures, but clearly observed as sharper peaks at low temperatures. In contrast, weaker carrier-phonon interaction in  $\text{Mo}_{0.5}\text{W}_{0.5}\text{Se}_2$  is not affecting these excitons at room temperature similar to previous reports of transition metal selenides [15–18] and tellurides [15, 18].

In conclusion, temperature-dependent reflectance spectroscopy, in conjunction with theoretical calculations, demonstrates various optically active transitions in bulk  $\text{Mo}_{0.5}\text{W}_{0.5}\text{S}_2$  and  $\text{Mo}_{0.5}\text{W}_{0.5}\text{Se}_2$  alloy single crystals. Apart from intra-, inter-layer and highly energetic  $A'$  and  $B'$  excitons, we also observe Rydberg excitons in both systems. Temperature-dependent studies show that at higher temperatures electron-phonon interactions strongly affect the higher-energy excitons than the lower-energy excitons. Our comprehensive study reveals these exotic excitonic states on a single platform, which will help to understand the fundamental physics and may open up the opportunities for the implementation of Bose-Einstein condensation, quantum information processing and optoelectronic applications at room temperature.

**Acknowledgments:** Authors gratefully acknowledge the Department of Science & Technology (Project no: DST/NM/TUE/QM-8/2019 (G)/1) and Science and Engineering Research Board (Project no: CRG/2019/002808) for financial support. We thankfully acknowledge central instrumentation and HPC facilities at IISER Bhopal.

- 
- [1] G. Wang, A. Chernikov, M. M. Glazov, T. F. Heinz, X. Marie, T. Amand, and B. Urbaszek, *Rev. Mod. Phys.* 90, 021001 (2018).
- [2] A. Chernikov, T. C. Berkelbach, H. M. Hill, A. Rigosi, Y. Li, B. Aslan, D. R. Reichman, M. S. Hybertsen, and T. F. Heinz, *Phys. Rev. Lett.* 113, 076802 (2014).
- [3] I. C. Gerber et al., *Phys. Rev. B* 99, 035443 (2019).
- [4] J. Horng, T. Stroucken, L. Zhang, E. Y. Paik, H. Deng, and S. W. Koch, *Phys. Rev. B* 97, 241404 (2018).
- [5] A. Arora et al., *Nat Commun* 8, 639 (2017).
- [6] C. Schneider, M. M. Glazov, T. Korn, S. Höfling, and B. Urbaszek, *Nat Commun* 9, 2695 (2018).
- [7] D. Y. Qiu, F. H. Da Jornada, and S. G. Louie, *Phys. Rev. Lett.* 111, 216805 (2013).
- [8] D. Xiao, G.-B. Liu, W. Feng, X. Xu, and W. Yao, *Phys. Rev. Lett.* 108, 196802 (2012).
- [9] C. Mai, A. Barrette, Y. Yu, Y. G. Semenov, K. W. Kim, L. Cao, and K. Gundogdu, *Nano Lett* 14, 202 (2014).
- [10] H. M. Hill, A. F. Rigosi, C. Roquelet, A. Chernikov, T. C. Berkelbach, D. R. Reichman, M. S. Hybertsen, L. E. Brus, and T. F. Heinz, *Nano Lett* 15, 2992 (2015).
- [11] S. Y. Chen et al., *Nano Lett* 19, 2464 (2019).
- [12] J. Shi, Z. Lin, Z. Zhu, J. Zhou, G. Q. Xu, and Q. H. Xu, *ACS Nano* 16, 15862 (2022).
- [13] K. R. Hansen, J. S. Colton, and L. Whittaker Brooks, *Advanced Optical Materials* 2301659 (2023).
- [14] S. Zheng, L. Sun, X. Zhou, F. Liu, Z. Liu, Z. Shen, and H. J. Fan, *Adv Opt Mater* 3, 1600 (2015).
- [15] A. R. Beal, J. C. Knights, and W. Y. Liang, *J. Phys. C: Solid State Phys.* 5, 3540 (1972).
- [16] W. Zhao, Z. Ghorannevis, L. Chu, M. Toh, C. Kloc, P. H. Tan, and G. Eda, *ACS Nano* 7, 791 (2013).
- [17] A. J. Grant, J. A. Wilson, and A. D. Yoffe, *Philosophical Magazine* 25, 625 (1972).
- [18] J. A. Wilson and A. D. Yoffe, *Adv Phys* 18, 193 (1969).
- [19] See the Supplemental Material (SM) for details of structural and compositional properties of bulk alloy single crystals, details of theoretical calculations and

- temperature-dependent reflectance spectroscopy, angle-resolved photoemission spectroscopy, Rydberg excitons in bulk alloy single crystals for other temperature, calculated absorption spectrum for monolayer alloys, and phonon dispersion curves.
- [20] A. F. Rigosi, H. M. Hill, K. T. Rim, G. W. Flynn, and T. F. Heinz, *Phys. Rev. B* 94, 075440 (2016).
- [21] G. Wang et al., *Nat Commun* 6, 10110 (2015).
- [22] H. Shi, R. Yan, S. Bertolazzi, J. Brivio, B. Gao, A. Kis, D. Jena, H. G. Xing, and L. Huang, *ACS Nano* 7, 1072 (2013).
- [23] X. Wang, G. Niu, J. Jiang, L. Sui, X. Zeng, X. Liu, Y. Zhang, G. Wu, K. Yuan, and X. Yang, *J. Phys. Chem. Lett.* 13, 10395 (2022).
- [24] P. D. Cunningham, A. T. Hanbicki, K. M. McCreary, and B. T. Jonker, *ACS Nano* 11, 12601 (2017).
- [25] A. Arora, K. Nogajewski, M. Molas, M. Koperski, and M. Potemski, *Nanoscale* 7, 20769 (2015).
- [26] J. Kang, Y. Wang, L. Zhou, O. A. Al-Hartomy, S. Wageh, Y. Wang, H. Zhang, S. Xiao, and J. He, *Appl Phys Lett* 123, 061107 (2023).
- [27] S. Biswas et al., *ACS Nano* 17, 7685 (2023).
- [28] Z. Wang, D. A. Rhodes, K. Watanabe, T. Taniguchi, J. C. Hone, J. Shan, and K. F. Mak, *Nature* 574, 76 (2019).
- [29] P. Taank, R. Karmakar, R. Sharma, R. K. Yadav, M. Shrivastava, N. C. Maurya, T. K. Maji, D. Karmakar, and K. V. Adarsh, *Journal of Physical Chemistry C* 126, 416 (2022).
- [30] D. Mandal, M. Shrivastava, S. Sharma, A. K. Poonia, S. Marik, R. P. Singh, and K. V. Adarsh, *ACS Appl Nano Mater* 5, 5479 (2022).
- [31] K. Bogaert, S. Liu, T. Liu, N. Guo, C. Zhang, S. GradeÅak, and S. Garaj, *Sci Rep* 8, 12889 (2018).
- [32] Z. Hemmat et al., *Advanced Materials* 32, 1907041 (2020).
- [33] P. Taank, A. Raji, R. S. Singh, and K. V. Adarsh, in *Conference on Lasers and Electro-Optics (Optica Publishing Group, San Jose, California, 2022)*, p. SF4K.6.
- [34] L. Wu et al., *ACS Nano* 15, 8397 (2021)
- [35] P. E. Blöchl, *Phys. Rev. B* 50, 17953 (1994).
- [36] G. Kresse and J. Furthmüller, *Phys. Rev. B* 54, 11169 (1996).
- [37] J. P. Perdew, K. Burke, and M. Ernzerhof, *Phys. Rev. Lett.* 77, 3865 (1996).
- [38] L. Bellaiche and D. Vanderbilt, *Phys. Rev. B* 61, 7877 (2000).
- [39] L. Hedin, *Phys. Rev.* 139, A796 (1965).
- [40] M. Shishkin and G. Kresse, *Phys. Rev. B* 74, 035101 (2006).
- [41] A. A. Mostofi, J. R. Yates, Y. S. Lee, I. Souza, D. Vanderbilt, and N. Marzari, *Comput Phys Commun* 178, 685 (2008).
- [42] V. Wang, N. Xu, J. C. Liu, G. Tang, and W.-T. Geng, *Comput Phys Commun* 267, 108033 (2021).
- [43] T. Cheiwchanchamnangij and W. R. L. Lambrecht, *Phys. Rev. B* 85, 205302 (2012).
- [44] H. Terrones, F. López-Uròas, and M. Terrones, *Sci Rep* 3, 1549 (2013).
- [45] J. Xiao, M. Zhao, Y. Wang, and X. Zhang, *Nanophotonics* 6, 1309 (2017).
- [46] E. E. Salpeter and H. A. Bethe, *Phys. Rev.* 84, 1232 (1951).
- [47] P. Taank, R. Karmakar, and K. V. Adarsh, *Surface and Interface Analysis* 55, 521 (2023).
- [48] E. Liu, J. Van Baren, T. Taniguchi, K. Watanabe, Y.-C. Chang, and C. H. Lui, *Phys. Rev. B* 99, 205420 (2019).
- [49] A. Raja et al., *Nano Lett* 18, 6135 (2018).
- [50] X. L. Yang, S. H. Guo, F. T. Chan, K. W. Wong, and W. Y. Ching, *Phys. Rev. A* 43, 1186 (1991).
- [51] T. Kazimierczuk, D. Fröhlich, S. Scheel, H. Stolz, and M. Bayer, *Nature* 514, 343 (2014).
- [52] V. V. Zalamai, N. N. Syrbu, I. G. Stamov, and S. I. Beril, *J. Opt.* 22, 085402 (2020).
- [53] K. Reimann, M. Steube, D. Fröhlich, and S. J. Clarke, *J Cryst Growth* 189-190, 652 (1998).
- [54] S. Faure, T. Guillet, P. Lefebvre, T. Bretagnon, and B. Gil, *Phys. Rev. B* 78, 235323 (2008).
- [55] G. Zhang, A. Chaves, S. Huang, F. Wang, Q. Xing, T. Low, and H. Yan, *Sci. Adv.* 4, eaap9977 (2018).
- [56] J. Deslippe, M. Dipoppa, D. Prendergast, M. V. O. Moutinho, R. B. Capaz, and S. G. Louie, *Nano Lett* 9, 1330 (2009).
- [57] A. R. Beal and W. Y. Liang, *J. Phys. C: Solid State Phys.* 9, 2459 (1976).
- [58] R. V. Kasowski, *Phys. Rev. Lett.* 30, 1175 (1973).
- [59] A. Togo, L. Chaput, T. Tadano, and I. Tanaka, *J. Phys.: Condens. Matter* 35, 353001 (2023).
- [60] Y. Ikeda, A. Carreras, A. Seko, A. Togo, and I. Tanaka, *Phys. Rev. B* 95, 024305 (2017).
- [61] K. Kaasbjerg, K. S. Thygesen, and K. W. Jacobsen, *Phys. Rev. B* 85, 115317 (2012).

## Supplemental Material

### **High-temperature observation of intralayer, interlayer, and Rydberg excitons in bulk van der Waals alloy single crystals**

Pravrati Taank<sup>1</sup>, Asif Ali<sup>1</sup>, Aravind Raji<sup>1</sup>, Ajay K. Poonia<sup>1</sup>, Matthew C. Beard<sup>2</sup>, Ravi Shankar Singh<sup>1\*</sup>, and K. V. Adarsh<sup>1\*</sup>

<sup>1</sup>*Department of Physics, Indian Institute of Science Education and Research, Bhopal 462066, India*

<sup>2</sup>*Chemistry & Nanoscience Center, National Renewable Energy Laboratory, Golden, Colorado 80401, USA*

#### **Corresponding Author\***

Email: [rssingh@iiserb.ac.in](mailto:rssingh@iiserb.ac.in) and [adarsh@iiserb.ac.in](mailto:adarsh@iiserb.ac.in)

#### **Contents:**

S1. Comparison with previous studies	2
S2. Structural and compositional properties of bulk alloy single crystals	3-7
S3. Theoretical calculations	8-9
S4. Angle-resolved photoemission spectroscopy (ARPES)	10-11
S5. Crystal structure	12
S6. Temperature-dependent reflectance spectroscopy	13
S7. Rydberg excitons in bulk alloy single crystals	14
S8. Assignment of A' and B' excitonic transitions	15
S9. Intra and interlayer excitons in TMDs	16
S10. Calculated absorption spectrum for monolayer alloys	17
S11. Phonon dispersion curves of bulk alloys	18
References	19

### S1. Comparison with previous studies

**Table S1.** Comparison with the previous reports on ground state optical absorption/reflection.

Sample	No. of layers	Temperature (K)	A (eV)	B (eV)	A' (eV)	B' (eV)	IX (eV)	References
MoS <sub>2</sub>	Monolayer	Room	✓	✓				[20], [22]
	Few layer, bulk		✓	✓				[3,22,23]
	Bilayer		✓	✓			✓	[3]
MoS <sub>2</sub>	Monolayer	Low	✓	✓				[3]
	Bi, trilayer		✓	✓			✓	[3]
	Bulk		✓	✓				[15]
WS <sub>2</sub>	Monolayer	Room	✓	✓				[20], [16], [24]
	Few layer		✓	✓				[23], [16]
	Bulk	Low	✓	✓				[15]
MoSe <sub>2</sub>	Monolayer	Room	✓	✓				[21]
	Mono, few layer	Low	✓	✓	✓	✓	✓	[25], [4]
	Bilayer		✓	✓			✓	[4]
Bulk	✓		✓	✓	✓	✓	[15], [4]	
WSe <sub>2</sub>	Monolayer	Room	✓	✓	✓	✓		[16], [21]
	Few layer		✓	✓	✓	✓		[16]
	Few layer	Low	✓	✓	✓	✓		[17]
Bulk	✓		✓	✓	✓		[15]	
MoWS <sub>2</sub>	Monolayer	Room	✓	✓				[20]
	Few layer		✓	✓				[23], [26]
	Bulk*		✓	✓	✓	✓		*present study
	Bulk*	Low	✓	✓	✓	✓	✓	*present study
MoWSe <sub>2</sub>	Monolayer	Room	✓	✓				[21]
	Bulk*		✓	✓	✓	✓	✓	*present study
	Bulk*	Low	✓	✓	✓	✓	✓	*present study



## S2. Structural and compositional properties of bulk alloy single crystals

### *X-ray diffraction (XRD):*

Room temperature XRD patterns of bulk  $\text{Mo}_{0.5}\text{W}_{0.5}\text{S}_2$  and  $\text{Mo}_{0.5}\text{W}_{0.5}\text{Se}_2$  alloy single crystals (procured from HQ Graphene) were recorded using PANalytical ‘Empyrean’ X-ray diffractometer with Cu  $K\alpha$  radiation (1.54 Å). XRD patterns illustrated in Figs. S1(a,b), revealing the presence of sharp peaks along the  $c$ -axis (0 0 2*l*), thereby confirming their single crystalline nature.

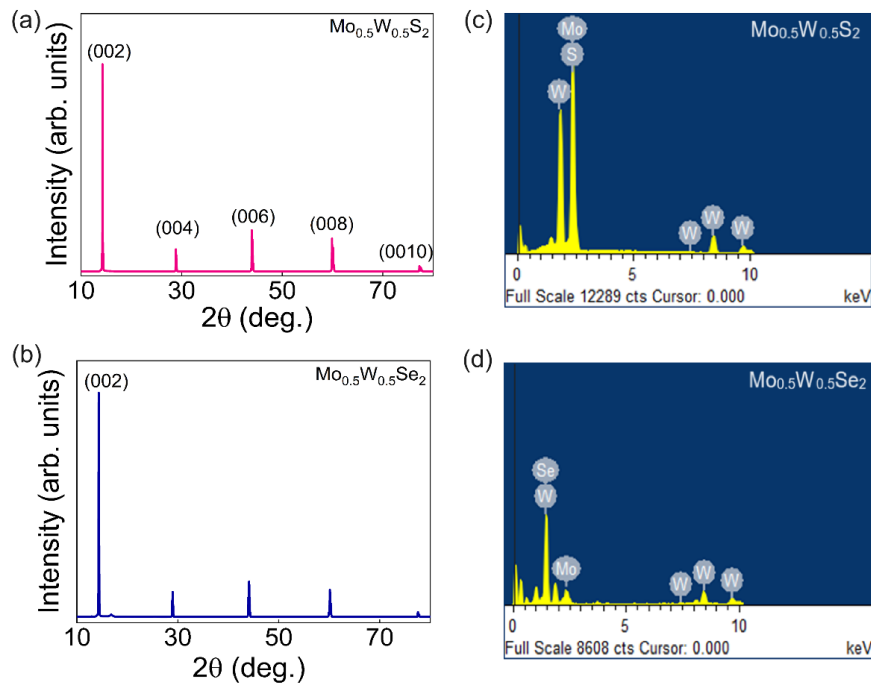


**FIG. S1.** XRD along the  $c$ -axis (0 0 2*l*) of bulk (a)  $\text{Mo}_{0.5}\text{W}_{0.5}\text{S}_2$  and (b)  $\text{Mo}_{0.5}\text{W}_{0.5}\text{Se}_2$  alloy single crystals. (c,d) EDX spectra confirm the uniform distribution of Mo and W with the atomic ratio of Mo:W = 1:1 in both alloys.

### *Scanning electron microscopy (SEM) and Energy-dispersive X-ray (EDX) spectroscopy:*

The layered structure of both single crystals was also observed through SEM images (Figs. S2 and S3). To estimate the elemental atomic ratio in bulk  $\text{Mo}_{0.5}\text{W}_{0.5}\text{S}_2$  and  $\text{Mo}_{0.5}\text{W}_{0.5}\text{Se}_2$  single

crystals, EDX measurements have been done. The overall error estimated in the measurements is less than 1%.

*a)  $Mo_{0.5}W_{0.5}S_2$  single crystal:*

EDX were taken from the region marked as pink box in the three SEM images as shown in Fig. S2 and estimated atomic weights of Mo, W, and S are presented in Table S2.

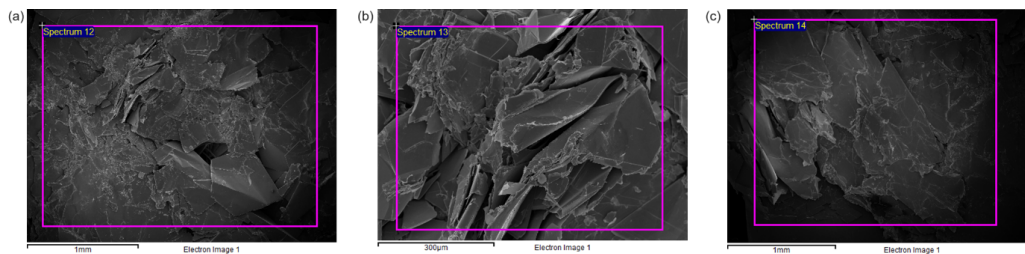


**FIG. S2.** SEM images for bulk  $Mo_{0.5}W_{0.5}S_2$  single crystals at three different positions.

**Table S2.** Extracted atomic weight for  $Mo_{0.5}W_{0.5}S_2$  single crystal

Position*	Elements	Weight %	Atomic %
A	S K	31.40	66.65
	Mo L	23.43	16.62
	W M	45.17	16.72
B	S K	31.76	67.03
	Mo L	23.29	16.43
	W M	44.95	16.55
C	S K	31.39	66.60
	Mo L	23.60	16.74
	W M	45.01	16.66
Overall Mo:W = $0.99 \pm 0.01$			

\*represents positions at different locations in the samples shown in Fig. S2.

*b)  $Mo_{0.5}W_{0.5}Se_2$  single crystal:*

EDX were taken from the region marked as pink box in the three SEM images as shown in Fig. S3 and estimated atomic weights of Mo, W, and Se are presented in Table S3.

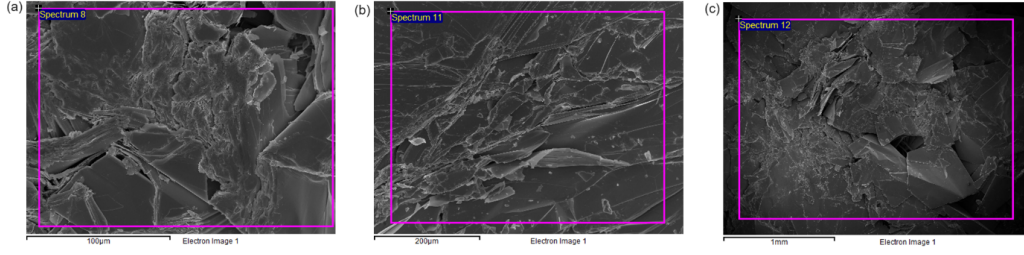


**FIG. S3.** SEM images for bulk  $\text{Mo}_{0.5}\text{W}_{0.5}\text{Se}_2$  single crystals at three different positions.

**Table S3.** Extracted atomic weight for  $\text{Mo}_{0.5}\text{W}_{0.5}\text{Se}_2$  single crystal

Position*	Elements	Weight %	Atomic %
A	Se K	52.87	66.73
	Mo L	15.55	16.15
	W M	31.58	17.12
B	Se K	52.84	66.59
	Mo L	15.89	16.48
	W M	31.27	16.92
C	Se K	52.84	66.92
	Mo L	14.90	15.53
	W M	32.26	17.54
Overall Mo:W = $0.93 \pm 0.04$			

The EDX spectra confirm the uniform distribution of Mo and W with the atomic ratio of Mo:W = 1:1 in both single crystals.

*X-ray photoemission spectroscopy (XPS):*

Room temperature XPS measurements were carried out using R4000 electron energy analyzer and monochromatic Al  $K\alpha$  ( $h\nu = 1486.6$  eV) photon source. Single crystals were cleaved in ultra-high vacuum (base pressure was below  $5 \times 10^{-11}$  mbar). The Fermi level and energy resolution of the spectrometer were measured by collecting the Fermi edge spectra of a polycrystalline Ag sample. The total energy resolution was  $\sim 300$  meV for XPS. The core-level

spectra of Mo, W, S, and Se for both  $\text{Mo}_{0.5}\text{W}_{0.5}\text{S}_2$  and  $\text{Mo}_{0.5}\text{W}_{0.5}\text{Se}_2$  single crystals are presented in Figs. S4(a,b), respectively. The sharpness of the core-level spectrum of all elements and the absence of additional features, for example, oxide peaks, provide conclusive evidence of the high purity of the single crystals.

The peak assignments with binding energy of all the elements are provided in Tables S4 and S5 for  $\text{Mo}_{0.5}\text{W}_{0.5}\text{S}_2$  and  $\text{Mo}_{0.5}\text{W}_{0.5}\text{Se}_2$  alloy single crystals, respectively. We have shifted our photoemission spectra to match the experimental valence band and density functional theory (DFT) results (Fig. 1 of the main manuscript), thereby aligning the Fermi level at the top of the valence band. Hence, binding energies in the valence band and core level XPS are with respect to the valence band maxima (VBM).

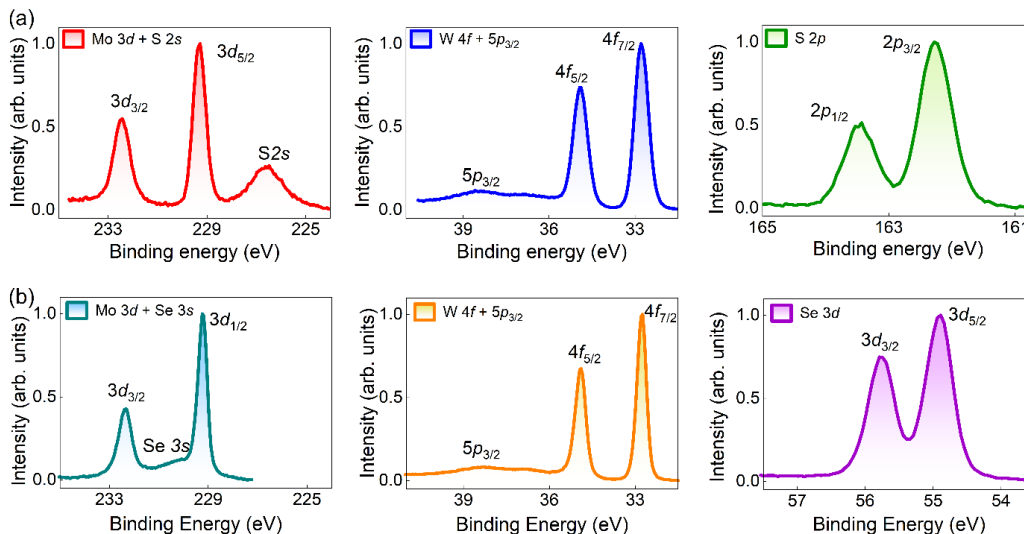


**FIG. S4.** XPS core-level spectrum of bulk (a)  $\text{Mo}_{0.5}\text{W}_{0.5}\text{S}_2$  and (b)  $\text{Mo}_{0.5}\text{W}_{0.5}\text{Se}_2$  single crystals confirming the high purity of the samples.

**Table S4.** Core-levels of elements with binding energy for Mo<sub>0.5</sub>W<sub>0.5</sub>S<sub>2</sub> single crystals.

Elements	Orbitals	Binding energy (eV)
Mo	$3d_{5/2}$	228.6
	$3d_{3/2}$	231.7
W	$4f_{7/2}$	31.7
	$4f_{5/2}$	33.8
	$5p_{3/2}$	37.2
S	$2s$	225.9
	$2p_{3/2}$	161.4
	$2p_{1/2}$	162.7

**Table S5.** Core-levels of elements with binding energy for Mo<sub>0.5</sub>W<sub>0.5</sub>Se<sub>2</sub> single crystals.

Elements	Orbitals	Binding energy (eV)
Mo	$3d_{5/2}$	228.1
	$3d_{3/2}$	231.2
W	$4f_{7/2}$	32.1
	$4f_{5/2}$	34.2
	$5p_{3/2}$	37.7
Se	$3s$	229.4
	$3d_{5/2}$	53.8
	$3d_{3/2}$	54.6

### S3. Theoretical calculations

#### *Density functional theory (DFT) calculations:*

Experimental lattice parameters were used for all calculations, and virtual crystal approximation (VCA) [38] was employed to represent the alloy compositions. A plane wave energy cutoff of 400 eV was used, and the effect of SOC was included in all the calculations. Electronic energy was minimized for a  $10^{-6}$  eV tolerance, and a Gaussian smearing of 0.05 eV was used. The Brillouin zone was sampled with a  $12 \times 12 \times 3$   $\Gamma$ -centered  $k$ -mesh. Electron energies, initially obtained from PBE calculations, were further refined through single-shot GW ( $G_0W_0$ ) calculations [39,40]. GW optimized pseudopotentials were used for all the calculations and response function cutoff of 266 eV was set for  $G_0W_0$ . A total of 240 bands, with 52 occupied bands, were considered for comprehensive analysis. The electronic band structures along high symmetry lines were obtained following Wannier interpolation techniques facilitated by the Wannier90 program [41].

#### *Comparison between virtual crystal approximation (VCA) and supercell method:*

Electronic band structures of bulk  $\text{Mo}_{0.5}\text{W}_{0.5}\text{S}_2$  and  $\text{Mo}_{0.5}\text{W}_{0.5}\text{Se}_2$  are calculated within VCA [38] and supercell method. In VCA, fractional compositions are considered at the M site, while in the case of the supercell method, a large supercells of a unit cell are used with Mo and W occupying 50% - 50% M sites. The supercell method is computationally expensive and requires a really large supercell to approximate a random distribution of Mo and W in alloy TMDs. Here, we compare the electronic structure calculated within these two methods, VCA (red) and supercell (blue), and show that they provide very similar results. In the supercell method, we chose an ordered structure with  $2 \times 2 \times 1$  supercell (Fig. S5(a)), and the band structure calculated for the supercell was unfolded in the primitive Brillouin zone. The calculated DFT band structures are presented in Figs. S5(b,c) for bulk  $\text{Mo}_{0.5}\text{W}_{0.5}\text{S}_2$  and  $\text{Mo}_{0.5}\text{W}_{0.5}\text{Se}_2$ , respectively. The band unfolding was performed using the VASPKIT [42] to compare the results of the two

methods. The similarity between the VCA results with the supercell method is clearly seen and justifies the use of VCA for further calculations including many-body  $G_0W_0$  and the Bethe-Salpeter equation (BSE).

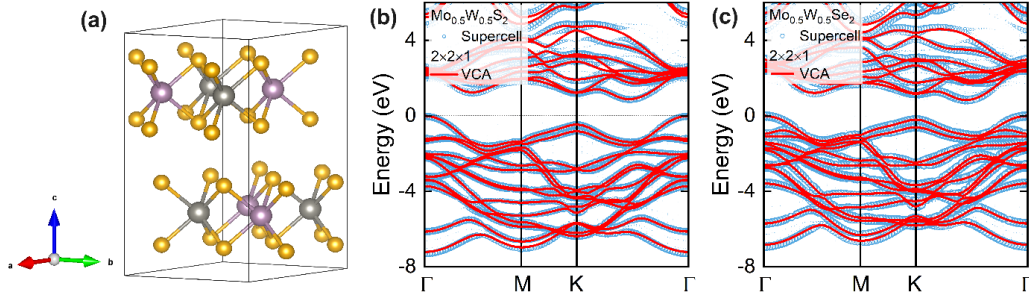


**FIG. S5.** (a) Supercell of  $2 \times 2 \times 1$  for  $\text{Mo}_{0.5}\text{W}_{0.5}(\text{S/Se})_2$ . The grey, purple, and yellow balls represent Mo, W, and S/Se, respectively. Electronic band structure calculated from VCA and supercell methods for bulk (b)  $\text{Mo}_{0.5}\text{W}_{0.5}\text{S}_2$  and (c)  $\text{Mo}_{0.5}\text{W}_{0.5}\text{Se}_2$ .

#### S4. Angle-resolved photoemission spectroscopy (ARPES)

To investigate valence band dispersion and spin-orbit coupling (SOC) driven band splitting at K valley, we have performed the ARPES measurements at room temperature using monochromatic He I ( $h\nu = 21.1$  eV) radiation. Single crystal of  $\text{Mo}_{0.5}\text{W}_{0.5}\text{Se}_2$  was *in-situ* cleaved. Fig. S6 shows the  $k$ -resolved band dispersion of  $\text{Mo}_{0.5}\text{W}_{0.5}\text{Se}_2$  along  $\bar{\Gamma}$ - $\bar{K}$  direction. The valence band at  $\bar{K}$  point exhibits SOC split bands with a splitting of  $\sim 0.37$  eV. The spectrum shows weak intensity at the VBM around the  $\bar{\Gamma}$  point. The ARPES spectrum was shifted to match to the energies of the top-most energy band, thus aligning the zero energy at the VBM. Constant energy cuts at two different energies, at 0 eV and -0.20 eV integrated within  $\pm 20$  meV energy region, are also shown in Fig. S6(c,d). Finite intensity can be seen around  $\bar{\Gamma}$  point at 0 eV cut, while for  $\bar{K}$  point finite intensity appears at about -0.20 eV cut, suggesting that VBM at  $\bar{K}$  point is lower by about 0.20 eV than the global VBM situated at  $\bar{\Gamma}$  point. Furthermore, we have included the energy distribution curve from ARPES, clearly showing the SOC splitting of the band of  $\sim 0.37$  eV at K valley (Fig. S6(d)). The overall band dispersion of  $\text{Mo}_{0.5}\text{W}_{0.5}\text{Se}_2$  is similar to that of parent bulk TMDs. The DFT (within VCA) calculated band structure (red line) for  $k_z = 0.25$  (out of plane momentum for He I radiation) overlaid over the ARPES spectrum shows a good agreement, suggesting that DFT is sufficient enough to capture the valence band characteristic in alloys. Notably, in the case of  $\text{Mo}_{0.5}\text{W}_{0.5}\text{S}_2$  single crystal, the flake size was smaller than the beam spot size, so we could not acquire reliable data.



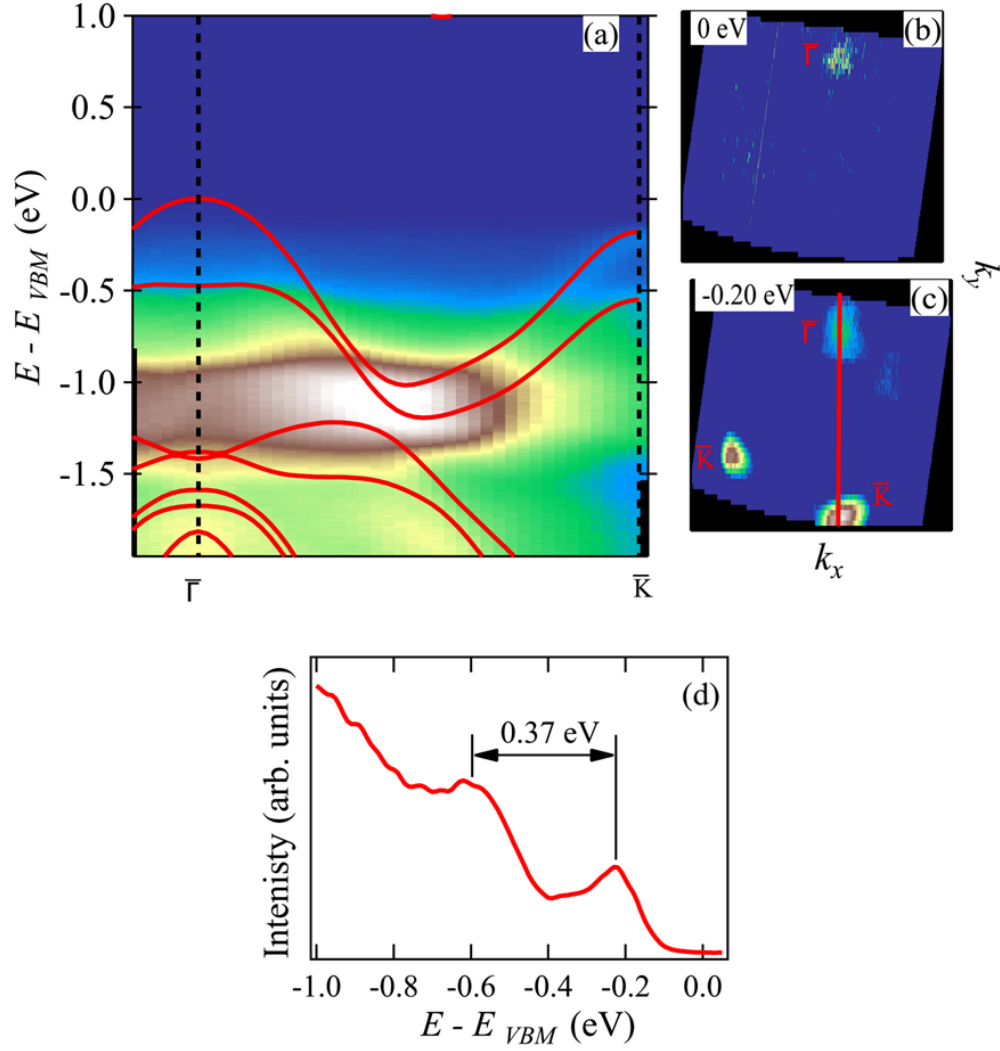


**FIG. S6.** (a) Room temperature ARPES spectrum of  $\text{Mo}_{0.5}\text{W}_{0.5}\text{Se}_2$  single crystal collected using He I radiation. DFT VCA calculated band dispersion for  $k_z = 0.25$  is represented by red lines. Constant energy cuts at (b) 0 eV and (c) -0.20 eV energies. The red line in (c) shows the cut along which the ARPES spectrum has been shown in (a). (d) Energy distribution curve from ARPES representing the SOC splitting of the band of  $\sim 0.37$  eV at the K valley.

## S5. Crystal structure

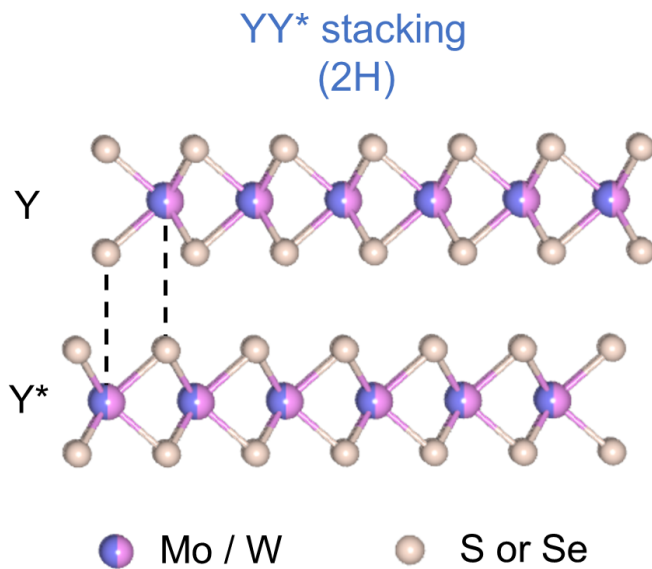


**FIG. S7.** Crystal structure of bulk alloy TMD single crystal representing the 2H phase with YY\* stacking. Here, Y consists of trigonal prismatic  $MX_6$  arranged in a hexagonal symmetry, while the  $Y^*$  is  $180^\circ$  in-plane rotated Y stacking.

### S6. Temperature-dependent reflectance spectroscopy

The surface roughness of the sample can affect the scattering of the reflected light; therefore, for correct measurements, a smooth, clean, and shining surface is required. In order to achieve it, both single crystals were cleaved using scotch tape before the measurements. To record the reflected signals, we used a tungsten-halogen lamp as a light source, which offers a broad spectrum in the UV-vis, and near-infrared (1.37-3.54 eV) regions. The sample was mounted in a closed-cycle exchange gas cryostat (Model number: SHI-950-7) at temperatures ranging from 4 to 300 K. The experiments were conducted in a vacuum of  $\sim 10^{-5}$  mbar. A temperature controller is used to change the temperature of the cryostat. Outside the cryostat, the white light was connected to an optical fiber. The experimental setup used in our study is shown in Fig. S8. The beam is steered into the cryostat with the help of mirrors and lenses. The reflected lights are collected using optical fiber and sent to Oceanview spectrometer to record the reflectance spectrum. The experiments on various pieces of samples have been performed multiple times at various positions on the sample surface, and the reproducibility of the results was ascertained.

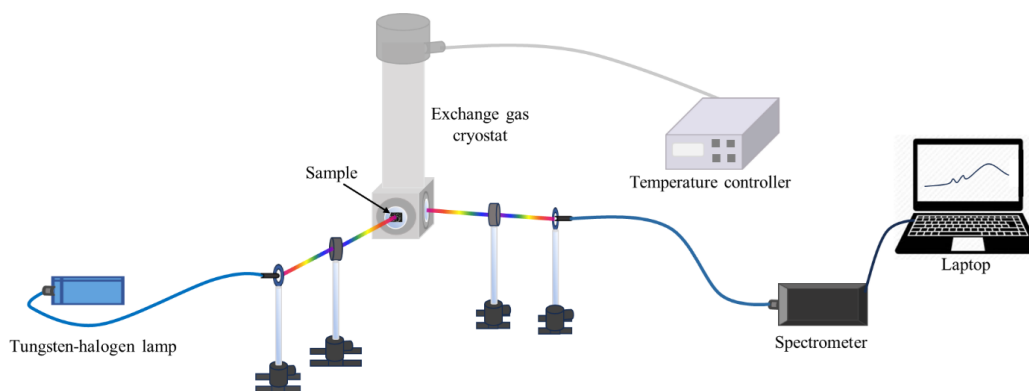


**Fig. S8.** Experimental set-up to measure temperature-dependent reflectance spectroscopy.

### S7. Rydberg excitons in bulk alloy single crystals

*Rydberg excitons in bulk  $\text{Mo}_{0.5}\text{W}_{0.5}\text{S}_2$  single crystal:*

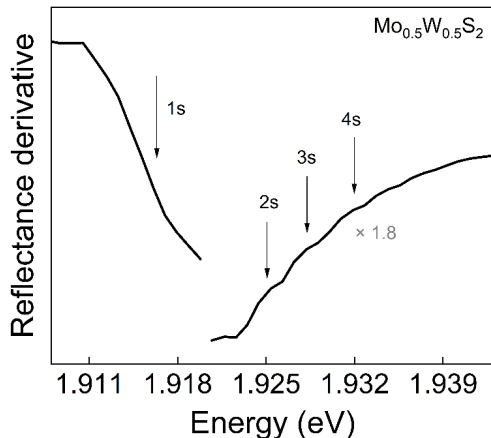


**FIG. S9.** The first derivative of the reflectance spectra calculated from BSE of bulk  $\text{Mo}_{0.5}\text{W}_{0.5}\text{S}_2$  single crystal. The arrows represent the exciton Rydberg series up to  $4s$  states.

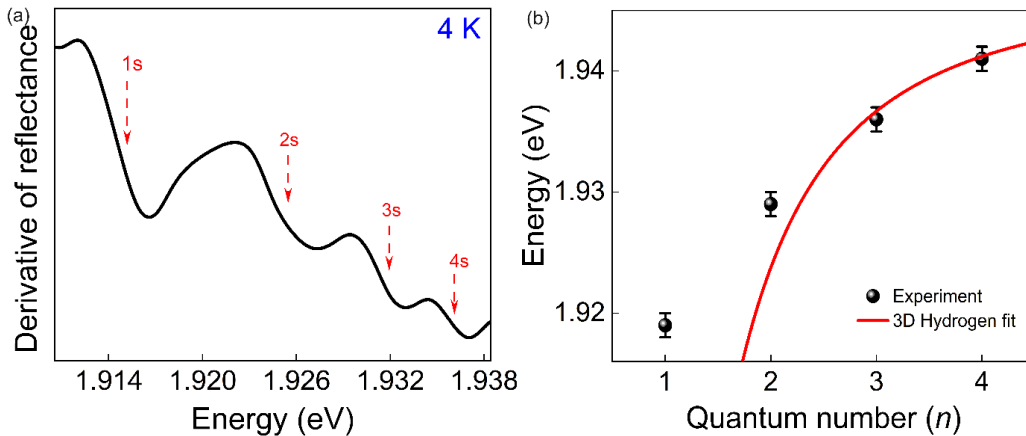


**FIG. S10.** (a) The first derivative of the experimentally measured reflectance spectrum of bulk  $\text{Mo}_{0.5}\text{W}_{0.5}\text{S}_2$  single crystal at 4 K. The peaks represent the exciton Rydberg series up to  $4s$  states, similar to 80 K data presented in the main manuscript. (b) Experimentally obtained the transition energies of the Rydberg series as a function of quantum number ( $n$ ). The  $n=3$ , and 4 peaks follow the 3D hydrogen model and the fit is represented by the red line. The reason for this nonhydrogenic behavior is described in the main manuscript.

### S8. Assignment of A' and B' excitonic transitions

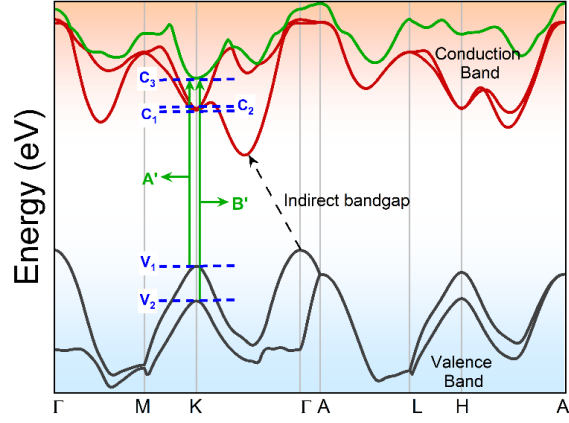


**FIG. S11.** Schematic figure of bulk TMD band structure and various optical transitions, presented here for clarity. The vertical transitions from  $V_1^{(\uparrow)} \rightarrow C_3^{(\uparrow)}$ , and  $V_2^{(\downarrow)} \rightarrow C_3^{(\downarrow)}$  results in the formation A' and B' excitons, respectively. Here,  $C_3$  is the spin degenerate band. The assignments of A' and B' excitons are based on experimental observations supported by the electronic band structure.

### S9. Intra and interlayer excitons in TMDs

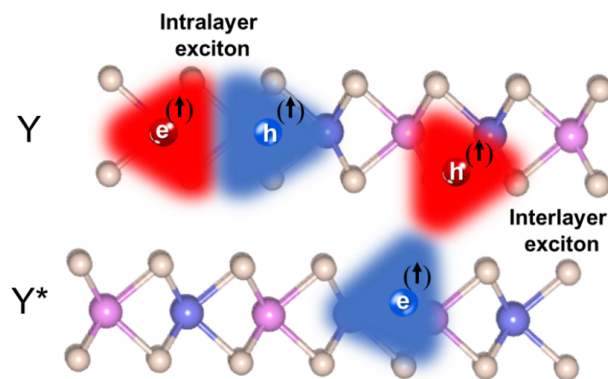


**FIG. S12.** Schematic representation of intralayer and IX excitons in TMDs. Intralayer excitons consist of an electron and a hole in the same layer whereas, for IX, the electron and hole are in different layers. The formation of both excitons is optically allowed only when spins of electron and hole (black arrows) are in the same orientation.

### S10. Calculated absorption spectrum for monolayer alloys

The calculations for monolayers were performed in a similar way as for bulk. We use the same in-plane lattice parameters for the monolayers and the size of the vacuum slab between two adjacent layers was 15 Å. Fig. S13 shows the optical absorption spectra for  $\text{Mo}_{0.5}\text{W}_{0.5}\text{S}_2$  and  $\text{Mo}_{0.5}\text{W}_{0.5}\text{Se}_2$  monolayers. A and B excitonic features are clearly observed with the splitting of about  $\sim 290$  and  $\sim 330$  meV. The excitonic peaks assigned to interlayer excitons (IXs) in the bulk are not found in the monolayers.

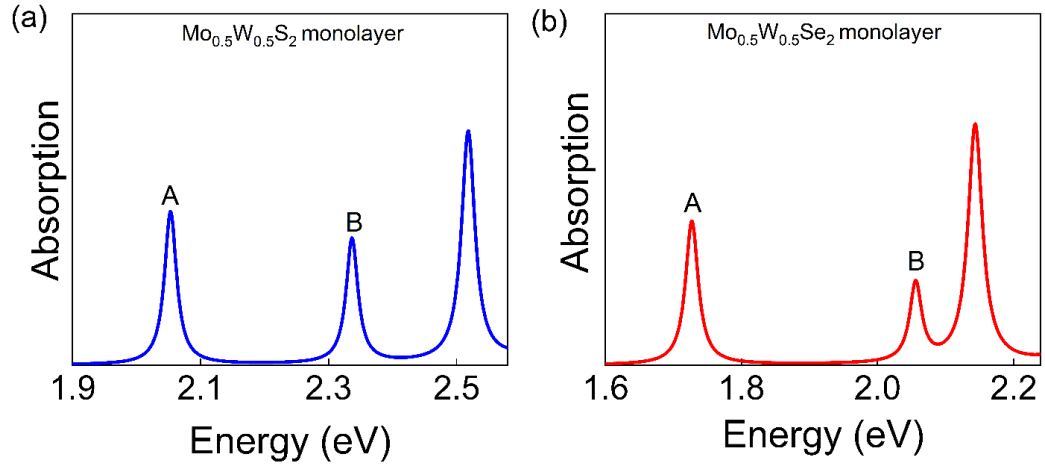


**FIG. S13.** Absorption spectrum obtained from BSE calculations of monolayer (a)  $\text{Mo}_{0.5}\text{W}_{0.5}\text{S}_2$  and (b)  $\text{Mo}_{0.5}\text{W}_{0.5}\text{Se}_2$ . Both spectra show the disappearance of IXs due to absence of interlayer interaction in monolayers.

### S11. Phonon dispersion curves of bulk alloys

Phonon dispersion curves for both systems were calculated for the ordered alloy structure ( $2 \times 2 \times 1$  supercell of the primitive cell) utilizing finite displacement method as implemented in PHONOPY code [59]. A  $2 \times 2 \times 2$  supercell (total 192 atoms) of the ordered structures with experimental lattice constants was used for phonon calculations. Unfolding of the phonon band structure within the Brillouin zone of the primitive cell was performed using UPHO code [60] and has been shown in Fig. S14. The longitudinal optical phonons appear at  $\sim 45$  meV for  $\text{Mo}_{0.5}\text{W}_{0.5}\text{S}_2$  and  $\sim 32$  meV for  $\text{Mo}_{0.5}\text{W}_{0.5}\text{Se}_2$  [61].

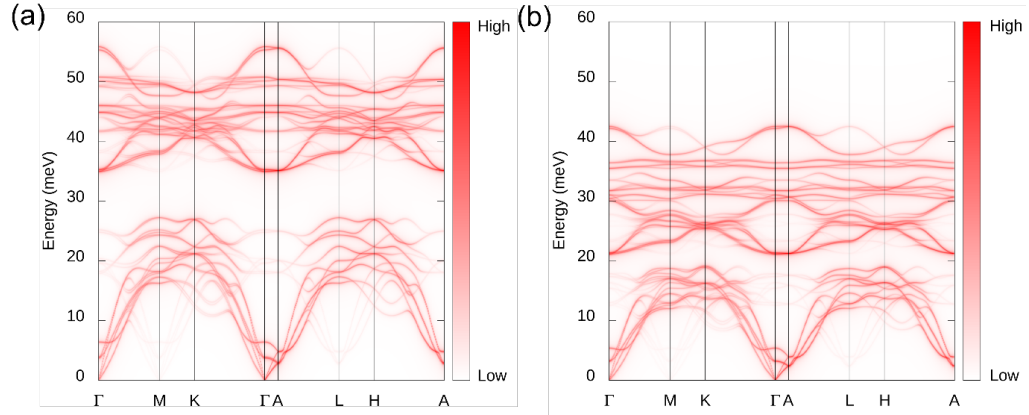


**FIG. S14.** Calculated phonon dispersion curves for bulk (a)  $\text{Mo}_{0.5}\text{W}_{0.5}\text{S}_2$  and (b)  $\text{Mo}_{0.5}\text{W}_{0.5}\text{Se}_2$ .



## References

- [3] I. C. Gerber et al., Phys. Rev. B **99**, 035443 (2019).
- [4] J. Horng, T. Stroucken, L. Zhang, E. Y. Paik, H. Deng, and S. W. Koch, Phys. Rev. B **97**, 241404 (2018).
- [15] A. R. Beal, J. C. Knights, and W. Y. Liang, J. Phys. C: Solid State Phys. **5**, 3540 (1972).
- [16] W. Zhao, Z. Ghorannevis, L. Chu, M. Toh, C. Kloc, P. H. Tan, and G. Eda, ACS Nano **7**, 791 (2013).
- [17] A. J. Grant, J. A. Wilson, and A. D. Yoffe, Philosophical Magazine **25**, 625 (1972).
- [20] A. F. Rigosi, H. M. Hill, K. T. Rim, G. W. Flynn, and T. F. Heinz, Phys. Rev. B **94**, 075440 (2016).
- [21] G. Wang et al., Nat Commun **6**, 10110 (2015).
- [22] H. Shi, R. Yan, S. Bertolazzi, J. Brivio, B. Gao, A. Kis, D. Jena, H. G. Xing, and L. Huang, ACS Nano **7**, 1072 (2013).
- [23] X. Wang, G. Niu, J. Jiang, L. Sui, X. Zeng, X. Liu, Y. Zhang, G. Wu, K. Yuan, and X. Yang, J. Phys. Chem. Lett. **13**, 10395 (2022).
- [24] P. D. Cunningham, A. T. Hanbicki, K. M. McCreary, and B. T. Jonker, ACS Nano **11**, 12601 (2017).
- [25] A. Arora, K. Nogajewski, M. Molas, M. Koperski, and M. Potemski, Nanoscale **7**, 20769 (2015).
- [26] J. Kang, Y. Wang, L. Zhou, O. A. Al-Hartomy, S. Wageh, Y. Wang, H. Zhang, S. Xiao, and J. He, Appl Phys Lett **123**, 061107 (2023).
- [38] L. Bellaiche and D. Vanderbilt, Phys. Rev. B **61**, 7877 (2000).
- [39] L. Hedin, *New Method for Calculating the One-Particle Green's Function with Application to the Electron-Gas Problem*, Phys. Rev. **139**, A796 (1965).
- [40] M. Shishkin and G. Kresse, Phys. Rev. B **74**, 035101 (2006).
- [41] A. A. Mostofi, J. R. Yates, Y. S. Lee, I. Souza, D. Vanderbilt, and N. Marzari, Phys Commun **178**, 685 (2008).
- [42] V. Wang, N. Xu, J. C. Liu, G. Tang, and W.-T. Geng, VASPKIT: Comput Phys Commun **267**, 108033 (2021).
- [59] A. Togo, L. Chaput, T. Tadano, and I. Tanaka, J. Phys.: Condens. Matter **35**, 353001 (2023).
- [60] Y. Ikeda, A. Carreras, A. Seko, A. Togo, and I. Tanaka, Phys. Rev. B **95**, 024305 (2017).
- [61] K. Kaasbjerg, K. S. Thygesen, and K. W. Jacobsen, Phys. Rev. B **85**, 115317 (2012).